Visible light photoacoustic ophthalmoscopy and near-infrared-II optical coherence tomography in the mouse eye

Cite as: APL Photon. 8, 106108 (2023); doi: 10.1063/5.0168091
Submitted: 17 July 2023 • Accepted: 10 October 2023 •
Published Online: 24 October 2023

R. Haindl,[1,2,3,a)] V. Bellemo,[3,4] P. Rajendran,[5] B. Tan,[3,4] M. Liu,[2,3] B. S. Lee,[6] Q. Zhou,[7] R. A. Leitgeb,[2] W. Drexler,[2] L. Schmetterer,[1,2,3,4,8,9,10] and M. Pramanik[11,b)]

AFFILIATIONS

[1]School of Chemistry, Chemical Engineering and Biotechnology, Nanyang Technological University, Singapore
[2]Centre for Medical Physics and Biomedical Engineering, Medical University of Vienna, Vienna, Austria
[3]Singapore Eye Research Institute, Singapore National Eye Centre, Singapore
[4]SERI-NTU Advanced Ocular Engineering (STANCE) Program, Nanyang Technological University, Singapore
[5]Department of Radiation Oncology, Stanford University, Stanford, California 94305, USA
[6]Lee Kong Chian School of Medicine, Nanyang Technological University, Singapore
[7]Department of Biomedical Engineering, University of Southern California, Los Angeles, California 90089, USA
[8]Ophthalmology and Visual Sciences Academic Clinical Program, Duke-NUS Medical School, National University of Singapore, Singapore
[9]Department of Clinical Pharmacology, Medical University Vienna, Vienna, Austria
[10]Institute of Molecular and Clinical Ophthalmology, Basel, Switzerland
[11]Department of Electrical and Computer Engineering, Iowa State University, Ames, Iowa 50011, USA

[a)]**Electronic mail:** richard.haindl@meduniwien.ac.at
[b)]**Author to whom correspondence should be addressed:** mano@iastate.edu.
URL: https://www.ece.iastate.edu/ece-directory/profile/mano/

ABSTRACT

Non-invasive imaging plays a crucial role in diagnosing and studying eye diseases. However, existing photoacoustic ophthalmoscopy (PAOM) techniques in mice have limitations due to handling restrictions, suboptimal optical properties, limited availability of light sources, and permissible light fluence at the retina. This study introduces an innovative approach that utilizes Rose Bengal, a contrast agent, to enhance PAOM contrast. This enables visualization of deeper structures, such as the choroidal vasculature and sclera in the mouse eye, using visible light. The integration of near-infrared-II (NIR-II) optical coherence tomography provides additional tissue contrast and insights into potential NIR-II PAOM capabilities. To optimize imaging, we developed a cost-effective 3D printable mouse eye phantom and a fully 3D printable tip/tilt mouse platform. This solution elevates PAOM to a user-friendly technology, which can be used to address pressing research questions concerning several ocular diseases, such as myopia, glaucoma, and/or age-related macular degeneration in the future.

I. INTRODUCTION

In modern medicine, non-invasive imaging techniques play a crucial role in improving diagnostic accuracy and monitoring treatment responses across various organs. Among these techniques, photoacoustic imaging (PAI) and optical coherence tomography (OCT) have emerged as promising tools due to their label-free and non-ionizing nature. PAI utilizes pulsed excitation lasers to record pressure waves generated by photon absorption in chromophores, enabling detailed morphological and functional assessment.[1,2] On the other hand, OCT captures cross-sectional tomographic images by measuring backscattered or back-reflected light, pro-

viding microstructural information about biological systems and materials.[3]

In the field of ophthalmology, many eye diseases involve abnormalities in the vasculature,[4] making PAI a valuable tool for obtaining vascular morphological and functional parameters in conjunction with the well-established scattering contrast provided by OCT.[5–7] However, both PAI and OCT face challenges when imaging deeper ocular structures in the visible and near-infrared-I window, such as the choroid and sclera.[8–10] These structures hold particular significance in myopia research, diagnosis, and treatment monitoring.[11–14] Recent studies have linked scleral extracellular matrix remodeling to axial elongation and a decrease in scleral strength and thickness, suggesting that high-resolution imaging of scleral structures may provide insights into the underlying mechanisms of this condition.[15,16] Although imaging human eyes using PAI remains challenging due to their size and the dampening effect of the large water volume on acoustic waves, mouse models of ocular diseases, including myopia, offer viable alternatives.[17]

In recent years, photoacoustic ophthalmoscopy (PAOM) has been developed for *in vivo* photoacoustic retinal imaging in rodents employing needle transducers.[7,9,18–23] However, the application of PAOM in mice has been limited by challenges associated with handling due to the small size of mouse eyes, their suboptimal optical properties, and the limited permissible light fluence at the retina. In this study, we present an innovative and user-friendly solution for deep imaging of the mouse eye *in vivo* using visible light PAOM. To expand the imaging depth range beyond the capabilities of existing systems, we introduced a contrast agent, Rose Bengal, which significantly enhanced PAOM contrast and enabled visualization of the choroidal vasculature and sclera. In addition, we integrated near-infrared-II OCT, which provides morphological tissue contrast and insights into the potential capabilities and penetration depth of future near-infrared-II (NIR-II) PAOM systems.

To ensure efficient and accurate imaging, we designed an animal handling solution that includes a fully 3D printable tip/tilt mouse platform and a 3D printable needle transducer holder. These

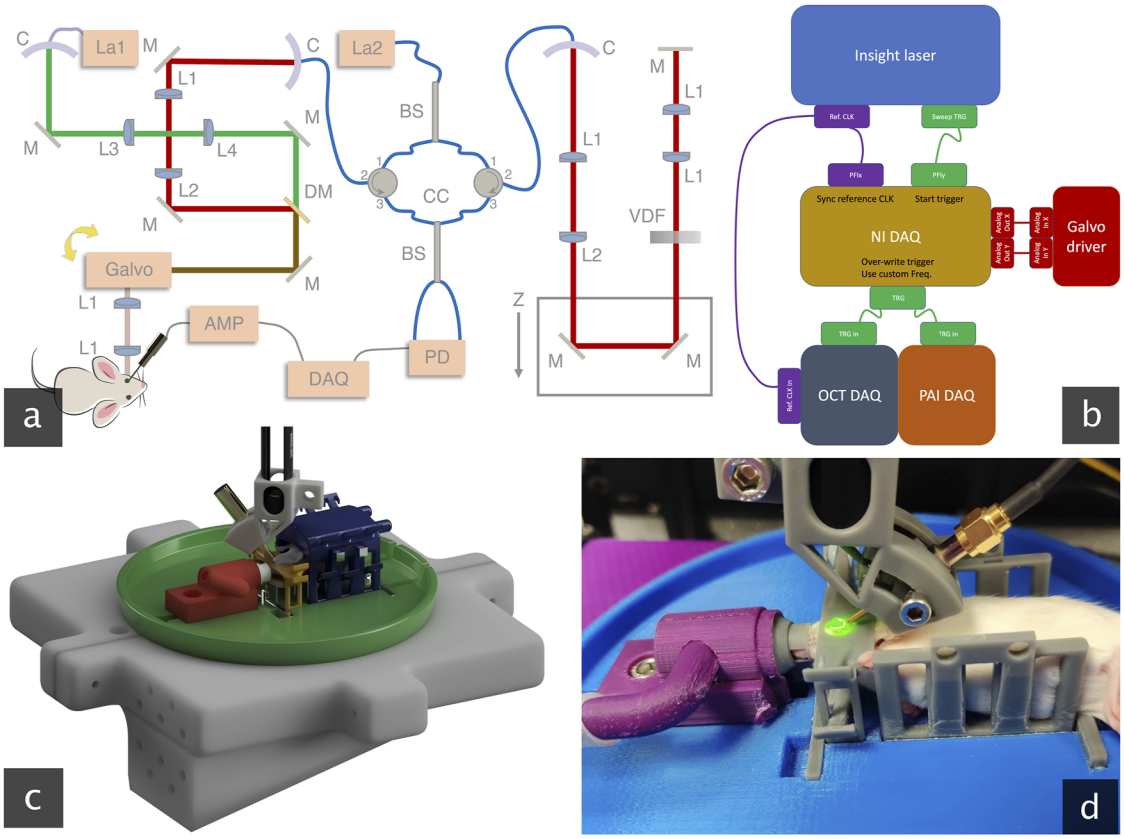

FIG. 1. Multimodal optical coherence photoacoustic ophthalmoscope (OC-PAOM). (a) Schematic of the OC-PAOM system, including the photoacoustic laser (La1) at 560 nm, OCT laser (La2) at 1310 nm, collimator (C), mirror (M), dichroic mirror (DM), lens (L), beam splitter (BS), circulator (CC), photodiode (PD), and variable density filter (VDF). The green path indicates the PAI excitation beam, the red path indicates the OCT laser beam, the brown path indicates the combined laser beam path, and the blue lines indicate the OCT fiber guide. The table lists the system specifications. (b) Schematic of the OC-PAOM data acquisition and trigger control, showing the purple path for the insight reference clock, the green path for trigger control, and the red path for galvanometric mirror control. (c) 3D printable mouse holder, including the gray base plate, green half sphere, red nose cone for anesthesia, yellow headrest, blue mouse restraint unit with water heating capability, and gold needle transducer with an arc mount in gray. (d) A picture of a mouse during an imaging session with the green PAOM laser and the needle transducer in contact with the eye.

components enable optimal transducer placement during imaging and facilitate seamless screening of the retina. Furthermore, we developed a cost-effective 3D printable mouse eye phantom with a ball lens compatible with the transducer holder to validate the functionality of the system, which may serve as a test phantom for small-animal PAOM systems.

This innovative imaging platform represents a significant advancement in pre-clinical ocular imaging using PAI and holds great potential for addressing pressing research questions related to high-frequency and critical ocular diseases, such as myopia, in the future.

II. METHODS

A. Hardware configuration

The multimodal ophthalmoscope integrates absorption contrast-based PAI with scattering contrast-based OCT using a dichroic short pass mirror. A diagram of the system design is shown in Fig. 1(a). The pulsed PAI excitation beam is tunable within the range of 559–576 nm and has a pulse repetition rate of 1–5 kHz. The excitation beam, emitted by a dye laser (La1, Credo-DYE-N, Sirah dye laser, Spectra Physics, Santa Clara, CA, USA) pumped with a 532 nm diode-pumped solid-state Nd:YAG laser (INNOSLAB BX-80-2, EdgeWave GmbH, Würselen, Germany), is coupled into a single mode fiber with a numerical aperture of 0.13 (460HP, Thorlabs GmbH, Dachau, Germany). A lens-based collimator (C, 47218, EdmundOptics, Barrington, New Jersey, United States) is employed to output a beam with a beam waist diameter of 1.68 mm. A variable lens-based telescope (L3, L4, AC127-030-AB, and AC127-025-AB, Thorlabs GmbH, Dachau, Germany) is utilized to compensate for refractive errors of the mouse eye, and the beam pulse energy can be adjusted up to 200 nJ at the sample, which was used for imaging, with a variable density filter before fiber coupling of the excitation light of La1. Details on the fiber coupling, dye laser setup, and refractive error compensation methods can be found in previous publications.[24,25]

The 1310 nm swept source OCT laser (SLE-101, Insight Photonic Solutions, Inc., Lafayette, Colorado) emits fiber coupled light, which enters a fiber-based 50:50 beamsplitter (BS, TW1300R5A2, Thorlabs GmbH, Dachau, Germany) to prepare for dual balanced detection of the OCT interference pattern.[26] The two exiting fibers are connected to circulators (CC, CIR-1310-50-APC, Thorlabs GmbH, Dachau, Germany), relaying the beams to the sample and reference arms, respectively. The third ports of the circulators eventually connect to the final 50:50 beamsplitter, generating the interference that is detected in a dual balanced photodetector (PD, PDB470C, Thorlabs GmbH, Dachau, Germany). The collimation of the sample arm beam is performed with a triplet collimator emitting a beam with a beam waist diameter of 1.11 mm (C, TC06APC-1310, Thorlabs GmbH, Dachau, Germany). A variable lens-based telescope (L1, L2, AC254-045-C-ML, and AC254-030-C-ML, Thorlabs GmbH, Dachau, Germany, Thorlabs) is used to compensate for refractive errors of the mouse eye. The reference arm comprises the same triplet collimator and lens pairs for hardware dispersion compensation purposes.[27] A variable density filter controls the power in the reference arm, and a translational stage controls the length of the optical path.

A dichroic mirror (DM, DMSP1000, Thorlabs GmbH, Dachau, Germany, Thorlabs) is used to combine the PAI and OCT beam paths. The combined beam is guided to the mouse eye using a telescope (L3, AC127-030-AB, Thorlabs GmbH, Dachau, Germany) to image the pivot point of the second galvanometric mirror onto the cornea of the mouse eye. The silver coated dual axis galvanometric scanners (Galvo, GVS002, Thorlabs GmbH, Dachau, Germany) raster scan the laser beam to achieve volumetric retinal imaging.

The high-frequency needle ultrasound transducer used in this study has a center frequency of 46 MHz and a −6 dB bandwidth of 27.3 MHz. Its characteristics were measured in a photoacoustic test chamber using aluminosilicate glass slides coated with 10 nm gold over a 2 nm Ti adhesion layer.[28] The transducer, with an aperture size of 0.5 mm, was fabricated in the Department of Biomedical Engineering of the University of Southern California using lead magnesium niobate–lead titanate (PMN-PT) as the active piezoelectric material and connected to a wideband low-power amplifier (24 dB gain, ZFL-500LN+, Mini-Circuits, New York, United States) before data readout with the PAI data acquisition (DAQ) card [Fig. 1(b)]. Detailed information on the optical coherence (OC)-PAOM system specifications is given in Table I.

B. Data acquisition and processing

The 1310 nm Insight swept OCT laser employs an internal sampling clock of 400 MHz and is configured to share a 10 MHz reference clock for synchronization purposes. This clock was used to synchronize the sampling of the 12 bit, 1 GS/s OCT data acquisition card DAQ (ATS9371, Alazar Technologies, Inc., Pointe-Claire, Quebec, Canada) with the laser sweep [Fig. 1(b), OCT DAQ].

The reference clock of an intermediate NI DAQ [Fig. 1(b), NI DAQ] card (National Instruments, PCI-6232, National Instruments Corp., Austin, Texas, United States) was synchronized to the laser reference clock [Fig. 1(b), PFIx] and served as a system control card. The laser's start sweep trigger was employed to synchronize the generation of a flexible A-scan trigger [Fig. 1(b), PFIy] with the movement of the galvanometer mirrors [Fig. 1(b), Analog Out X, Y].

TABLE I. System specifications. Theoretical diffraction limited intraocular resolution and step size are provided. A typical pupil diameter of 0.8 mm[29] and a refractive index for the retina of 1.38 at 1310 nm[30] are assumed. Lateral resolution is calculated according to Gaussian optics.[31]

Modality	ν and λ	Bandwidth	Axial res. (μm)	Lat. res. (μm)	Lat. step (μm)	A-line rate (kHz)
PAOM	46 MHz	27.3 MHz	23.6	2.7	1.6	1–4
OCT	1310 nm	75 nm	10	6.8	1.6	50

This type of synchronization was specifically chosen to achieve the most precise synchronization between the movement of the galvanometer mirrors and the OCT data acquisition. This is achieved because both the analog output and the generated A-scan trigger start at the same clock cycle in the NI DAQ clock. Furthermore, this configuration enables seamless multimodal integration, as it permits, for example, running the OCT acquisition at the same rate as PAI (in this case, 4 kHz), even simultaneously. By providing additional trigger signals, multiple modalities can also be synchronized at different repetition rates.

The 16 bit PAI DAQ (M4i.4420, Spectrum Instrumentation, Ahrensfelder Weg 13, 22927 Großhansdorf, Germany) was operated at the maximum sampling rate of 250 MS/s. The internal sampling clock of the card was used for data acquisition, while the NI DAQ generated trigger [Fig. 1(b), TRG] was used to start the data acquisition of every A-scan and to trigger the PAI laser pulse emission.

The OCT and PAI DAQ cards were connected to the PCI-e slots and the NI DAQ to the peripheral component interconnect (PCI) slot of a personal computer. LabVIEW (version 2021, National Instruments Corp., Texas, United States) was used as a programming language for data acquisition and display. PAI postprocessing was implemented in Python, version 3.7.14,[32] and the following libraries: matplotlib,[33] NumPy,[34] OpenCV,[35] and SciPy.[36] En face projections were generated with the software Fiji,[37] where the StackReg plugin was utilized to compensate for axial and minor lateral motion artifacts.[38] OCT postprocessing employed the programming language MATLAB, version R2020b (MathWorks, Inc., California, United States). Standard OCT signal processing (background subtraction, resampling, and fast Fourier transform) was used to reconstruct the depth profile.[39] Postprocessing of a volume took approximately one minute for each modality employing an AMD Ryzen Threadripper 3970X and multi-core processing.

C. Transducer arc mount

The needle transducer arc mount enables flexible angular alignment of the needle transducer with respect to the animal eye or ball lens of the mouse eye phantom, allowing high flexibility and optimization possibilities to maximize image quality and field of view for *in vivo* and phantom PAOM imaging. The transducer can be aligned between 35° and 60° toward the optical axis. The arc mount case is designed to optimize resin use with openings to the body of the case. The arc mount can be attached to a lens tube via an M6 screw and corresponding nut. The arc glider, inserted into the case, holds the transducer, which can be inserted into the top hole of the glider. An M4 screw holds the transducer in place, while another M4 screw secures the arc glider within the mounting case. An exploded view of the arc mount and glider is shown in Fig. 2(a).

A fully 3D printable mouse eye model was developed for use with both imaging modalities. The model was printed in black resin [Fig. 2(b)] with a Formlabs stereolithography printer (Form 3+, Somerville, Massachusetts, United States) and designed using Fusion 360 software (AUTODESK, San Rafael, California, United States). The base of the phantom is a half sphere with a diameter of 1 in., and a handle is attached to the base for easy rotation. The axis of rotation is at the imaging site, allowing the needle transducer to remain in place while the phantom rotates [Fig. 2(c)]. A small N-BK7 ball lens (No. 43-710, EdmundOptics, Barrington, New Jersey, United States) with a diameter of 2.5 mm was secured to the phantom using a bezel mount [Fig. 2(d)]. The distance from the lens to the focal spot of the 560 and 1310 nm beams was simulated using the Zemax software. Ultrasound gel was used for coupling. The OC-PAOM imaging results demonstrated good image quality and overlap between OCT and PAI without the need for focus adjustment [Fig. 2(f)]. The image shows a multimodal en face projection within the red outlined region of interest in Fig. 2(e).

D. Animals

The mice utilized in the present study were subjected to considerate care in accordance with the official ethics protocol and procedures as described therein. The Institutional Animal Care and Use Committee (NTU-IACUC) at Nanyang Technological University was the responsible local ethics body overseeing animal experimentation. The ethical protocol for conducting animal activities was assigned the reference number A19101.

An outbred albino mouse strain of the "IcrTac:ICR, Female" variety was employed for all experimental procedures. The mice were between 8 and 16 weeks of age and were housed in an animal

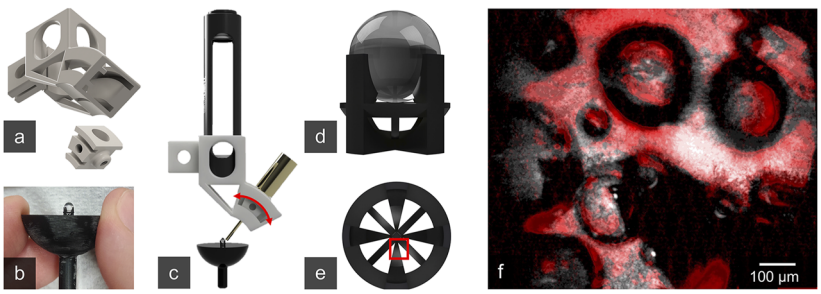

FIG. 2. Transducer arc mount with mouse eye phantom. (a) The transducer arc mount with a separated glider designed to hold and secure the needle transducer. (b) A side view of the 3D printed and assembled mouse eye phantom. (c) The fully assembled and attached arc mount with an inserted glider and needle transducer (gold), firmly fixed at the SM05 lens tube of the OC-PAOM sample arm. The needle transducer can be rotated along the focus area of the optical beam without losing contact with the ball lens (red arrow). (d) A side view of the bezel with the ball lens. (e) A top view of the phantom structure without the lens, where the red rectangle indicates the imaging area. (f) An OCT en face image (gray) overlaid with a PAI en face image (red) with trapped air bubbles.

facility, where they were provided with environmental enrichment to reduce anxiety.[40]

E. Imaging procedure

The animals were randomly selected, retrieved from the animal facility, and conveyed to the imaging location directly before the start of the experiment. Subsequently, the mice were subjected to anesthesia with isoflurane (2%–3%) and oxygen in the small rodent chamber of an anesthesia machine. Upon initial anesthesia, the mice were transferred to the 3D printed mouse holder equipped with a nose cone, headrest, and bite bar [Fig. 1(c)]. The anesthesia was then redirected to the nose cone to sustain the mouse's anesthetized state throughout the procedure. An artificial tear solution was utilized to moisturize the eye, and a zero-diopter contact lens (Advanced Vision Technologies, Lakewood, United States) was placed on the eyeball to prevent corneal dehydration and clouding, ensuring consistent imaging results.[41] The artificial tear solution was intermittently reapplied every 5 min.

The holder, along with the mouse, was subsequently mounted onto the holder mount and adjusted for optimal imaging quality [Fig. 1(d)], wherein a region of interest was preselected utilizing the fast OCT imaging system. Continuous PAI fast scans (200 × 200 pixels) were conducted to optimize the transducer position and the height of the animal holder, subsequently leading to the optimization of the imaging quality for the ensuing PAI slow scan (1000 × 1000 pixels). The field of view was set to 840 × 840 μm^2 to ensure a lateral scanning step size below the lateral resolution of the scanning beam on the retina (Table I) and to keep the acquisition time for the PAOM slow scan below 5 min (250 s). Parallel data acquisition is possible in this system, but data acquisition was conducted sequentially due to laser safety considerations (OCT immediately after PAI).

Following the imaging procedure, the mice were euthanized by administering an overdose of pentobarbital (100 mg/kg) via the intraperitoneal route. The euthanasia was further confirmed by a cervical dislocation. The animal was eventually disposed of in accordance with the established standard procedure.

III. RESULTS

A. OC-PAOM imaging and 3D printable mouse holder

The 3D printable mouse holder is composed of three primary components: a base [gray big part in Fig. 1(c)], a half sphere [green part in Fig. 1(c)], and attached modules [red, yellow, and blue parts in Fig. 1(c)]. The base is 270 × 270 mm^2 in size, with a hole mount diameter of 170 mm at its largest point, and consists of four parts assembled with seven M6 screws. One portion of the base includes additional holes and a mounting plate for secure attachment to a translational stage (XR25P-K2/M, Thorlabs GmbH, Dachau, Germany).

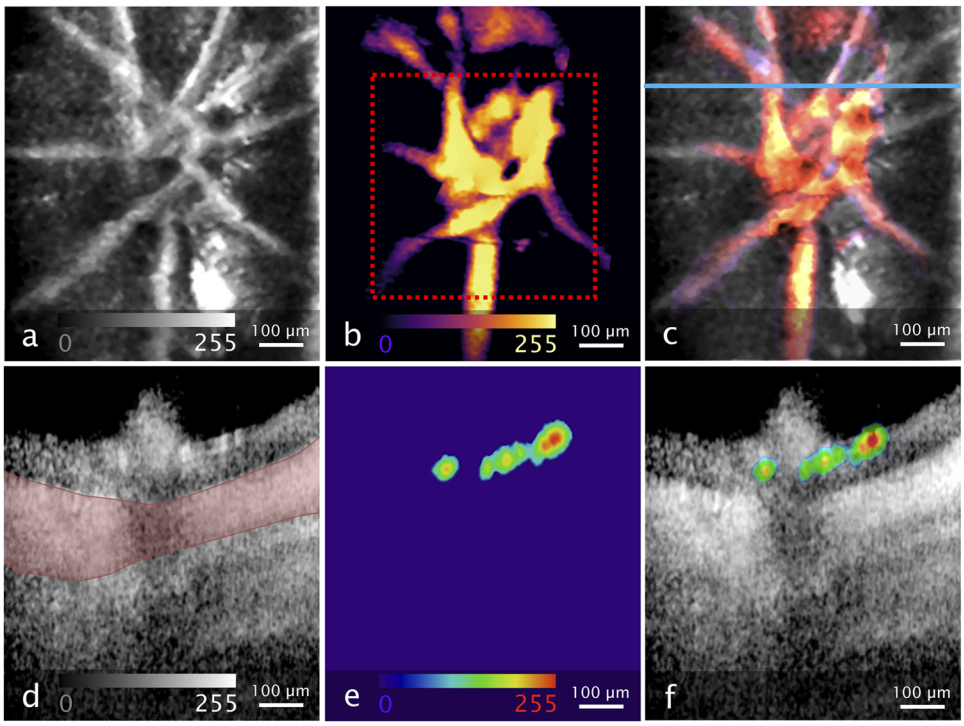

FIG. 3. Multimodal OC-PAOM imaging results. (a) An en face average intensity OCT projection of the nerve head region. (b) An en face maximum intensity PAOM projection of the same region. Dotted red square: active area of the ultrasound transducer. (c) Multimodal OC-PAOM en face projections, with PAOM in color. (d)–(f) OCT, PAOM, and OC-PAOM B-scans at the indicated position in (c) (blue line). Red shaded area: choroid. OCT and PAOM en face projections in (a)–(c) are generated at the depth of the retinal vasculature and after 3D median filtering of the acquired volume. The scale bar is valid for all spatial directions.

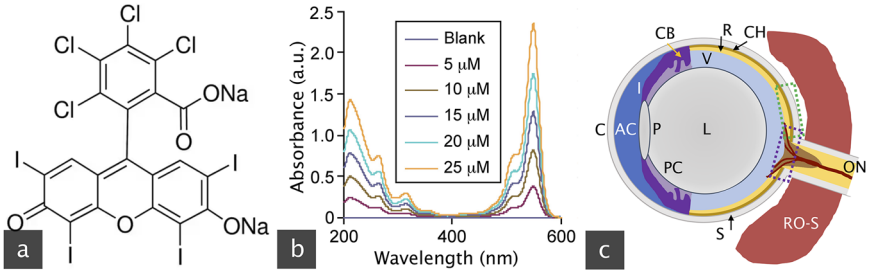

FIG. 4. Structure and application of Rose Bengal. (a) The chemical structure of Rose Bengal disodium salt. (b) UV–Vis absorbance spectra of different concentrations of Rose Bengal. The credit for the absorbance spectra goes to Raja and Barron. Minor modifications were made under the CC BY 4.0 license. (c) Cross-sectional sketch of a mouse eye with indicated imaging locations. Purple: imaging region around the optic nerve head, and green: imaging region for the Rose Bengal injection. RO-S with syringe: Rose Bengal injection into the retro-orbital sinus. ON: optic nerve. S: sclera. CH: choroid. R: retina. L: lens. P: pupil. CB: ciliary body. V: vitreous humor. PC: posterior chamber. AC: anterior chamber. I: iris. C: cornea.

The mouse holder half sphere has a diameter of 180 mm at its widest point and features engravings to accommodate the removable modules. This design allows for easy cleaning and modification of the modules, potentially saving production costs and time. The coarse parts, including the base, the half sphere, and the nose cone holder, were 3D printed with a polylactic (PLA) filament printer (Dremel 3D-20-01, Racine, Wisconsin, United States). The smaller modular parts, such as the bite bar, headrest, and mouse restraining unit, were printed using a stereolithography (SLA) printer (Form 3+, Formlabs, Somerville, Massachusetts, United States). A 3D rendering of the mouse holder is provided in the supplementary material.

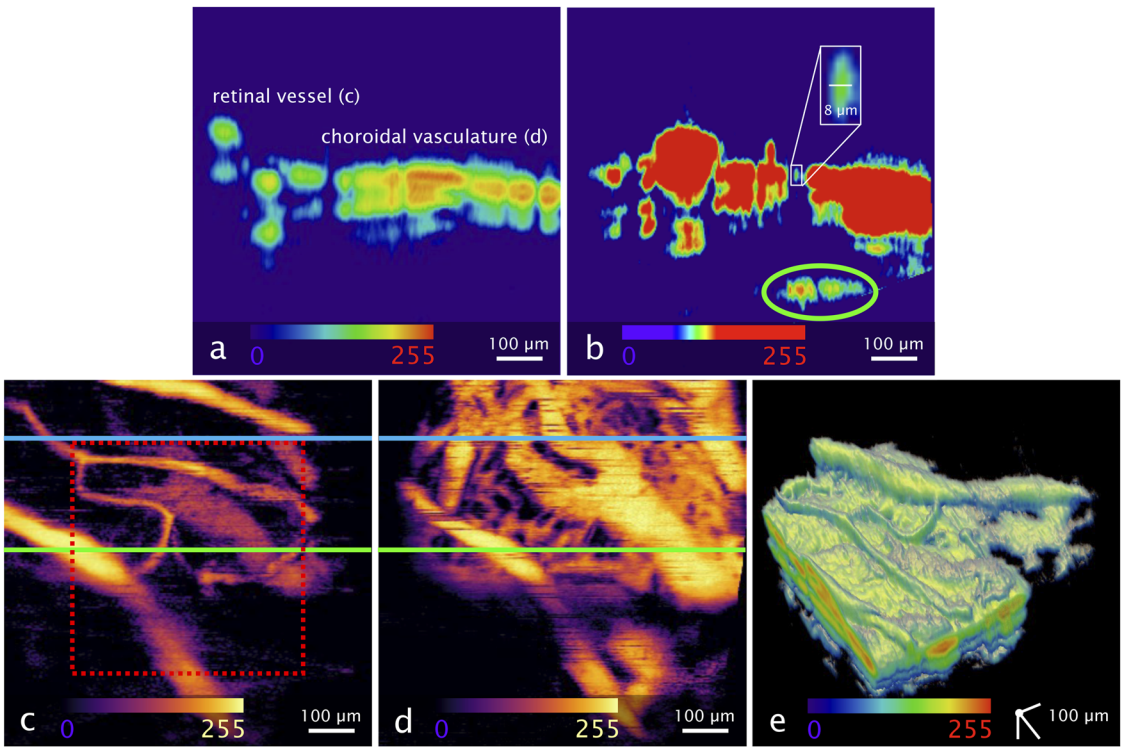

FIG. 5. Rose Bengal PAOM imaging. (a) A typical PAOM B-scan. (b) Contrast adjusted PAOM B-scan with unobstructed scleral features (green ellipse). (c) and (d) En face projections of the same volume at different depths for the retinal (c) and choroidal (d) layers, respectively. Dotted red square: active area of the ultrasound transducer. Blue line: B-scan position of (a). Green line: B-scan position of (b). (e) Volumetric rendering depicting the retinal vasculature on top of the choroid. The scale bar for (a)–(d) is valid for all spatial directions.

Figure 1(d) shows the assembled mouse holder during imaging, including the headrest and restraining unit. In addition, the assembly includes a lid (not illustrated), which features a water channel for artificial heating or cooling. The headrest is secured using rubber bands, and the restraining unit is also supported by rubber bands. The lid is removable and can be attached using M4 screws. The ICR mouse is held in the restraining unit, with its head secured in the headrest and its eye positioned at the center of rotation of the half sphere holder. The needle transducer is pointed toward the retina, and the mouse can be adjusted accordingly (rotation, tip, and tilt).

Imaging of ICR mice was performed using the 3D printed mouse mount. Figure 3 represents the en face [Figs. 3(a)–3(c)] and B-scan [Figs. 3(d)–3(f)] imaging results of OCT and PAOM modalities. The multimodal en face images in Fig. 3(c) depict the optic nerve head [dotted purple region in Fig. 4(c)] of the mouse and show that the two modalities are consistent in visualizing the vasculature emerging from the nerve head. PAOM provided high contrast, displaying emerging vessels in high detail, while OCT showed additional morphological contrast. With deep penetration achievable with NIR-II OCT imaging, the B-scan image in Fig. 3(d) demonstrated OCT's ability to visualize multiple layers from the inner limiting membrane to the retinal pigment epithelium (above the red band), the choroid (red band), and the sclera below the red band.[42] The acquisition time for PAOM was longer than OCT, taking 250 s, while OCT took 20 s.

B. PAOM imaging with Rose Bengal

Rose Bengal [Fig. 4(a)] is a contrast agent commonly used in ophthalmology to diagnose ocular surface disorders, such as keratitis and dry eye disease. This FDA-approved diagnostic stain belongs to the xanthene class of dyes, is characterized by tetraiodo-substitution,[43] and has a high absorption coefficient within the visible green light region close to 560 nm [Fig. 4(b)], making it suitable for imaging procedures such as the visible light PAOM developed in this study. Although sodium fluorescein is generally preferred for angiography,[44] Rose Bengal has been shown to induce collagen cross-linking,[45] which is promising for myopia treatment. Therefore, we decided to evaluate the benefits of using Rose Bengal (198250, Merck KGaA, Darmstadt, Germany) for PAOM imaging quality and penetration depth. A 0.1% w/v stock solution of Rose Bengal was prepared using water as a solvent, as higher concentrations have exhibited inherent cell toxicity.[46] The dye solution was administered via retro-orbital sinus injection, delivering a volume of 150 μl to the retinal vasculature [Fig. 4(c), RO-S].[47]

B-scan images obtained following a retrobulbar injection of 0.1% Rose Bengal [indicated by the dotted green region in Fig. 4(c)] revealed enhanced acoustic intensity and absorption not only in the retina but also in the choroid [Fig. 5(a)] and sclera [Fig. 5(b), marked in green], enabling the visualization of small, deep structures. Moreover, Rose Bengal-assisted retinal imaging exhibited an expanded field of view surpassing the active area of the transducer ($500 \times 500\ \mu m^2$) and allowed for the visualization of small vessels connected to larger branches in the maximum intensity en face projection of the retinal layer [Fig. 5(c)]. The demarcation between retinal and choroidal vasculature was discernible [Fig. 5(a)], and volumetric rendering is shown in Fig. 5(e), underscoring the high axial resolution achieved through the utilization of high-frequency sensor technology.

In addition, the maximum intensity en face projection of the choroidal layer visualizes the capillary system within the choroid with micrometer transverse resolution [Figs. 5(b) and 5(d)]. Notably, the visualization of the choroidal microvasculature was exclusively observed following Rose Bengal injection, highlighting its potential advantage for PAOM.

IV. DISCUSSION

Ocular rodent animal imaging plays a vital role in preclinical research due to the similarities between rodent models and humans.[48–50] Imaging techniques provide valuable insights into various diseases, and in this study, we introduced a novel concept for a rodent holder that allows rotation without repositioning the rodent's translational position. This innovative design facilitates imaging within the limited field of view accessible with PAOM. In addition, we developed a needle transducer holder that meets the stringent positional and alignment requirements of the transducer and excitation beam path. By demonstrating the efficacy of the fully 3D printable holder, we obtained imaging results of the mouse eye's retina, choroid, and sclera using multimodal OC-PAOM imaging, both with and without exogenous contrast.

With PAOM, we were able to image the nerve head region and achieve highly detailed visualization of the choroidal vasculature. NIR-II OCT provided access to the retina, choroid, and sclera, demonstrating its feasibility to penetrate through the choroid with lower vascular extinction at this wavelength. This suggests that NIR-II PAOM could be used to study scleral diseases, especially with the aid of contrast agents such as gold nanorods, in future investigations.[51] Notably, Rose Bengal emerged as a potent dye for PAOM with green excitation light, enabling visualization of the choroidal vasculature and sclera in mice for the first time.

The choice of Rose Bengal as a contrast agent was driven by its spectroscopic and photochemical properties. Rose Bengal exhibits a strong propensity for intersystem crossing, leading to the generation of a photochemically active triplet excited state upon laser light exposure.[43] This process produces reactive oxygen species (ROS) that can react with collagen fibril molecules, promoting the formation of new chemical bonds through photopolymerization. Consequently, tissue mechanical strength increases, enhancing its stiffness. This property shows promise for increasing the stiffness of scleral tissue, which may have implications for myopia treatment.[52] Hence, Rose Bengal proves to be a versatile and theranostic contrast agent, and its effectiveness in PAOM opens new avenues for studying ocular diseases and their treatment.

However, as Rose Bengal-induced photothrombosis is a commonly employed method for creating a model of retinal vein occlusion (RVO) under specific illumination conditions, it is important to discuss potential issues with RVO in our study. First, in our imaging experiments, we did not observe any morphological changes indicative of RVO in the vasculature, such as vessel blurring and reduced contrast.[53] We utilized 200 nJ pulses at the cornea and a repetition rate of 4 kHz, resulting in an average illumination power of 0.8 mW at 560 nm. However, the undiluted aperture of the mouse eye (0.8 mm) limits the deposited energy on the retina to 96 nJ. This value closely approaches the American National Standards Institute (ANSI Z136.1-2022) limit of the maximum permissible single laser pulse energy of 77 nJ if a human retina were involved. Following,

calculations indicated an average energy density of 1.7 J/cm^2 at the retina during imaging, which is significantly lower than what is typically used for RVO induction with a green laser and Rose Bengal. In addition, the Rose Bengal concentrations employed in our study (1 mg/ml) were lower than those in established RVO studies.[54] Consequently, we do not anticipate RVO occurrences in our imaging setup.

To provide further insights, it is important to note that Rose Bengal-assisted RVO and photothrombosis are typically induced either through repeated pulsed illumination lasting roughly 0.2–0.5 s for each pulse[53] or through continuous laser illumination lasting several minutes.[55] These methods involve large spot sizes ranging from 50 to 400 μm, high power green lasers (20–200 mW), and a high concentration of Rose Bengal (15–50 mg/ml). In studies using repeated illumination, the respective energy density ranges between 1.7 and 7.6 kJ/cm^2, which is three orders of magnitude higher than the energy density used in our study.[53,56,57]

For studies employing continuous illumination, visible blood clots typically appear after continuous laser illumination lasting 1 min.[58] Sullender *et al.*[59] utilized a 532 nm laser in a stroke model with 200 mW patterned illumination for 420 s on an area of 0.09 mm^2. Assuming an energy density for continuous illumination using the formula

$$\textit{Energy density}\ (\mathrm{J/cm^2}) = \frac{\textit{Power}\ (\mathrm{W}) * \textit{exposure time}\ (\mathrm{s})}{\textit{Area}\ (\mathrm{cm^2})}$$

results in an energy density of 93 kJ/cm^2. In contrast, Clark *et al.*[60] employed a similar patterned illumination method with a lower laser power of 20 mW for 30 s and an illumination area of 0.15 mm^2, yielding an energy density of 400 J/cm^2, ~240 times higher than in our study.

With the exception of a study utilizing multiphoton femtosecond laser illumination with 87 mW at 1000 nm, a 25× objective, and 5 min of illumination time,[61] photothrombosis has not been studied with short pulsed lasers, particularly not with nanosecond (ns) pulsed lasers that provide only an individual short pulse of light at a small focal area at a time, as in our study. Additional investigations in this area represent an interesting research topic for future experiments.

Previous studies have employed PAOM without contrast agents to investigate ocular models in mice, rats, and rabbits.[62,63] While mice and rats have small eyes, rabbits resemble human eyes in size. However, rabbits lack a fovea, and their retinal vasculature differs from that of humans and rodents. Moreover, rabbits possess a unique horizontal streak of myelinated retinal nerve fiber layer called the medullary ray, absent in humans and rodents.[64] Nevertheless, rabbits have been successfully utilized to study ocular diseases such as choroidal vascular occlusions (CVO) using multimodal PAOM and OCT imaging systems, allowing visualization, characterization, and quantification of laser-induced CVO with high resolution and contrast.[56] Similarly, integrated PAOM and OCT systems have been employed to study retinal and choroidal vessels, retinal vein occlusion, and retinal neovascularization in rabbits.[65–70] In rats, PAOM combined with scanning laser ophthalmoscopy, optical coherence tomography, and fluorescein angiography has been used to visualize the choroidal vasculature in albino rats, but not in pigmented rats.[18,21,71] In addition, PAOM with near-infrared-I (NIR-I) excitation has enabled visualization of the choroidal vasculature in rats, albeit with lower quality in the imaged retinal vasculature compared to visible light excitation.[9] Multi-wavelength illumination has also been employed for quantifying the metabolic rate of oxygen.[19] However, research on mice using PAOM remains limited,[20] and until now, PAOM has not been able to resolve the choroidal vasculature or sclera in mice, which our study successfully achieved.

The utilization of NIR-II OCT for retinal imaging is not commonly reported in the scientific literature due to inherent challenges associated with high water absorption and limited axial resolution, leading to limited previous reports.[30,72–75] Nevertheless, our system employs a high-power swept source, overcoming the limitations of NIR-II OCT and enabling deep imaging in this wavelength range. This allows direct observation of the sclera without the need for surgery or imaging from the side of the eye globe, offering advantages in terms of throughput, long-term studies, and animal welfare. The illumination power of OCT at the cornea was 15 mW. This is below the maximum permissible exposure for humans of 499 mW for the retina and 118.7 mW for the cornea (ANSI Z136.1-2022).

The presence of retinal degeneration in ICR mice presented difficulties for OCT imaging as it interferes with the visualization of normal retinal layer structure due to morphological changes in the retina.[73,76] In ICR mice, retinal degeneration manifests as diffuse atrophy, reduced thickness, and the absence of photoreceptor layers. The inner nuclear layer also exhibits cellular deficiencies, including nuclear shrinkage and loss.[77] This shrinkage causes the choroid to be situated at a depth of 150–250 μm.[73] Nevertheless, despite these pathological alterations, the objectives of our study were unaffected. NIR-II OCT imaging was primarily employed to investigate deep imaging capabilities extending to the sclera, provide a morphological reference for PAOM, and expedite the identification of the region of interest for PAOM imaging. In addition, we aimed to evaluate the potential penetration depth for potential NIR-II PAOM imaging.

In future studies, we aim to further enhance the 3D printed mouse eye phantom. Its current limitation lies in the ease with which air bubbles can be trapped when using ultrasound gel. Such inclusions could be prevented by incorporating a water reservoir, as preliminary tests have shown that water does not introduce air bubbles but leads to rapid drying and, consequently, a shorter imaging window. Furthermore, we plan to replace the PAOM excitation laser with a faster model that offers a higher tunability of the wavelength range, allowing access to longer wavelengths for deeper scleral imaging. We will explore different exogenous contrast agents to enhance scleral contrast in myopic mouse models, furthering our understanding of myopia disease onset and progression. Moreover, we will target scleral cross-linking, as previously demonstrated with green light,[78] by combining treatment and monitoring with PAOM using the same light source.

V. CONCLUSION

Our study provides a comprehensive solution for imaging deeper structures of the mouse eye *in vivo* by combining PAOM with contrast agents, integrating NIR-II OCT, and addressing animal handling restrictions with a novel 3D printable platform and phantom. The ocular imaging platform has the potential to be

used to answer pressing research questions concerning several high-frequency and critical epidemic ocular diseases, such as myopia, in the future.

SUPPLEMENTARY MATERIAL

A video of a 360° 3D rendering of the mouse holder is provided in the supplementary material.

ACKNOWLEDGMENTS

We thank Rhonnie Austira Dienzo for the useful discussion and help regarding animal imaging and René Werkmeister for providing support and overseeing the laser safety calculations. This work was funded by grants from the National Medical Research Council (Grant Nos. CG/C010A/2017-SERI, OFLCG/004c/2018-00, MOH-000249-00, MOH-000647-00, MOH-001001-00, MOH-001015-00, MOH-000500-00, MOH-000707-00, MOH-001072-06, and MOH-001286-00), the National Research Foundation Singapore (Grant Nos. NRF2019-THE002-0006 and NRF-CRP24-2020-0001), A*STAR (Grant No. A20H4b0141), the Singapore Eye Research Institute and Nanyang Technological University [SERI-NTU Advanced Ocular Engineering (STANCE) Program], and the SERI-Lee Foundation (Grant No. LF1019-1), Singapore. M. Liu is funded by the H2020-MSCA-IF-2019 project SkinOptima with Grant Agreement No. 894325.

AUTHOR DECLARATIONS

Conflict of Interest

The authors have no conflicts to disclose.

Ethics Approval

Ethics approval for experiments reported in the submitted manuscript on animal or human subjects was granted. The mice utilized in the present study were subjected to considerate care and in accordance with the official ethics protocol and procedures as described therein. The Institutional Animal Care and Use Committee (NTU-IACUC) at Nanyang Technological University was the responsible local ethics body overseeing the animal experimentation. The ethical protocol for conducting animal activities was assigned the reference number A19101.

Author Contributions

R. Haindl: Conceptualization (equal); Data curation (lead); Formal analysis (lead); Investigation (lead); Methodology (lead); Project administration (equal); Software (lead); Visualization (lead); Writing – original draft (lead); Writing – review & editing (lead). **V. Bellemo**: Data curation (equal); Investigation (supporting); Resources (equal); Software (equal); Writing – review & editing (equal). **P. Rajendran**: Conceptualization (supporting); Methodology (equal); Validation (equal); Writing – review & editing (equal). **B. Tan**: Conceptualization (supporting); Resources (equal); Validation (equal); Writing – review & editing (equal). **M. Liu**: Investigation (equal); Validation (equal); Writing – review & editing (equal). **B. S. Lee**: Investigation (equal); Validation (equal); Writing – original draft (supporting); Writing – review & editing (equal). **Q. Zhou**: Resources (equal); Writing – review & editing (equal). **R. A. Leitgeb**: Conceptualization (equal); Methodology (equal); Supervision (supporting); Writing – original draft (supporting); Writing – review & editing (equal). **W. Drexler**: Resources (equal); Supervision (supporting); Writing – review & editing (supporting). **L. Schmetterer**: Conceptualization (equal); Funding acquisition (lead); Investigation (equal); Resources (equal); Writing – review & editing (equal). **M. Pramanik**: Conceptualization (equal); Funding acquisition (lead); Investigation (equal); Project administration (equal); Resources (equal); Supervision (equal); Validation (equal); Writing – review & editing (equal).

DATA AVAILABILITY

The data that support the findings of this study are available from the corresponding author upon reasonable request.

REFERENCES

[1] D. Das, A. Sharma, P. Rajendran, and M. Pramanik, "Another decade of photoacoustic imaging," Phys. Med. Biol. **66**, 05TR01 (2021).
[2] S. Manohar and D. Razansky, "Photoacoustics: A historical review," Adv. Opt. Photonics **8**, 586–617 (2016).
[3] R. A. Leitgeb, F. Placzek, E. A. Rank, L. Krainz, R. Haindl, Q. Li, M. Liu, M. Andreana, A. Unterhuber, T. Schmoll, and W. Drexler, "Enhanced medical diagnosis for dOCTors: A perspective of optical coherence tomography," J. Biomed. Opt. **26**, 100601 (2021).
[4] R. A. Leitgeb, R. M. Werkmeister, C. Blatter, and L. Schmetterer, "Doppler optical coherence tomography," Prog. Retinal Eye Res. **41**, 26–43 (2014).
[5] A. de la Zerda, Y. M. Paulus, R. Teed, S. Bodapati, Y. Dollberg, B. T. Khuri-Yakub, M. S. Blumenkranz, D. M. Moshfeghi, and S. S. Gambhir, "Photoacoustic ocular imaging," Opt. Lett. **35**, 270–272 (2010).
[6] R. Haindl, W. Trasischker, A. Wartak, B. Baumann, M. Pircher, and C. K. Hitzenberger, "Total retinal blood flow measurement by three beam Doppler optical coherence tomography," Biomed. Opt. Express **7**, 287–301 (2016).
[7] S. Jiao, M. Jiang, J. Hu, A. Fawzi, Q. Zhou, K. K. Shung, C. A. Puliafito, and H. F. Zhang, "Photoacoustic ophthalmoscopy for *in vivo* retinal imaging," Opt. Express **18**, 3967–3972 (2010).
[8] T. Fujiwara, Y. Imamura, R. Margolis, J. S. Slakter, and R. F. Spaide, "Enhanced depth imaging optical coherence tomography of the choroid in highly myopic eyes," Am. J. Ophthalmol. **148**, 445–450 (2009).
[9] T. Liu, Q. Wei, W. Song, J. M. Burke, S. Jiao, and H. F. Zhang, "Near-infrared light photoacoustic ophthalmoscopy," Biomed. Opt. Express **3**, 792–799 (2012).
[10] B. Tan, V. A. Barathi, E. Lin, C. Ho, A. Gan, X. Yao, A. Chan, D. W. Wong, J. Chua, G. S. Tan, and L. Schmetterer, "Longitudinal structural and microvascular observation in RCS rat eyes using optical coherence tomography angiography," Invest. Ophthalmol. Visual Sci. **61**, 54 (2020).
[11] T. R. Fricke, M. Jong, K. S. Naidoo, P. Sankaridurg, T. J. Naduvilath, S. M. Ho, T. Y. Wong, and S. Resnikoff, "Global prevalence of visual impairment associated with myopic macular degeneration and temporal trends from 2000 through 2050: Systematic review, meta-analysis and modelling," Br. J. Ophthalmol. **102**, 855–862 (2018).
[12] B. Holden, P. Sankaridurg, E. Smith, T. Aller, M. Jong, and M. He, "Myopia, an underrated global challenge to vision: Where the current data takes us on myopia control," Eye **28**, 142–146 (2014).
[13] Y. Imamura, T. Iida, I. Maruko, S. A. Zweifel, and R. F. Spaide, "Enhanced depth imaging optical coherence tomography of the sclera in dome-shaped macula," Am. J. Ophthalmol. **151**, 297–302 (2011).
[14] Y. Ma, X. Qu, X. Zhu, X. Xu, J. Zhu, P. Sankaridurg, S. Lin, L. Lu, R. Zhao, L. Wang, H. Shi, H. Tan, X. You, H. Yuan, S. Sun, M. Wang, X. He, H. Zou, and N. Congdon, "Age-specific prevalence of visual impairment and refractive error in

children aged 3–10 years in Shanghai, China," Invest. Ophthalmol. Visual Sci. **57**, 6188–6196 (2016).
[15]N. Mehta and A. Wen, "Myopia: A global epidemic," Retina Today 52–55 (2019).
[16]I. G. Morgan, A. N. French, R. S. Ashby, X. Guo, X. Ding, M. He, and K. A. Rose, "The epidemics of myopia: Aetiology and prevention," Prog. Retinal Eye Res. **62**, 134–149 (2018).
[17]X. Jiang, T. Kurihara, H. Kunimi, M. Miyauchi, S.-i. Ikeda, K. Mori, K. Tsubota, H. Torii, and K. Tsubota, "A highly efficient murine model of experimental myopia," Sci. Rep. **8**, 2026 (2018).
[18]T. Ma, X. Zhang, C. T. Chiu, R. Chen, K. Kirk Shung, Q. Zhou, and S. Jiao, "Systematic study of high-frequency ultrasonic transducer design for laser-scanning photoacoustic ophthalmoscopy," J. Biomed. Opt. **19**, 016015 (2014).
[19]W. Song, Q. Wei, W. Liu, T. Liu, J. Yi, N. Sheibani, A. A. Fawzi, R. A. Linsenmeier, S. Jiao, and H. F. Zhang, "A combined method to quantify the retinal metabolic rate of oxygen using photoacoustic ophthalmoscopy and optical coherence tomography," Sci. Rep. **4**, 6525 (2014).
[20]W. Song, Q. Wei, L. Feng, V. Sarthy, S. Jiao, X. Liu, and H. F. Zhang, "Multimodal photoacoustic ophthalmoscopy in mouse," J. Biophotonics **6**, 505–512 (2013).
[21]Q. Wei, T. Liu, S. Jiao, and H. F. Zhang, "Image chorioretinal vasculature in albino rats using photoacoustic ophthalmoscopy," J. Mod. Opt. **58**, 1997–2001 (2011).
[22]Z. Xie, S. Jiao, H. F. Zhang, and C. A. Puliafito, "Laser-scanning optical-resolution photoacoustic microscopy," Opt. Lett. **34**, 1771–1773 (2009).
[23]P. Zhang, M. Goswami, A. Zam, E. N. Pugh, and R. J. Zawadzki, "Effect of scanning beam size on the lateral resolution of mouse retinal imaging with SLO," Opt. Lett. **40**, 5830–5833 (2015).
[24]D. J. Harper, M. Augustin, A. Lichtenegger, P. Eugui, C. Reyes, M. Glösmann, C. K. Hitzenberger, and B. Baumann, "White light polarization sensitive optical coherence tomography for sub-micron axial resolution and spectroscopic contrast in the murine retina," Biomed. Opt. Express **9**, 2115–2129 (2018).
[25]M. Moothanchery and M. Pramanik, "Performance characterization of a switchable acoustic resolution and optical resolution photoacoustic microscopy system," Sensors **17**, 357 (2017).
[26]Z. Chen, E. Rank, K. M. Meiburger, C. Sinz, A. Hodul, E. Zhang, E. Hoover, M. Minneman, J. Ensher, P. C. Beard, H. Kittler, R. A. Leitgeb, W. Drexler, and M. Liu, "Non-invasive multimodal optical coherence and photoacoustic tomography for human skin imaging," Sci. Rep. **7**, 17975 (2017).
[27]R. Haindl, M. Duelk, S. Gloor, J. Dahdah, J. Ojeda, C. Sturtzel, S. Deng, A. Joyce Deloria, Q. Li, M. Liu, M. Distel, W. Drexler, and R. Leitgeb, "Ultra-high-resolution SD-OCM imaging with a compact polarization-aligned 840 nm broadband combined-SLED source," Biomed. Opt. Express **11**, 3395–3406 (2020).
[28]S. Deng, R. Haindl, E. Zhang, P. Beard, E. Scheuringer, C. Sturtzel, Q. Li, A. J. Deloria, H. Sattmann, R. A. Leitgeb, Y. Yuan, L. Schmetterer, M. Pramanik, M. Distel, W. Drexler, and M. Liu, "An optical coherence photoacoustic microscopy system using a fiber optic sensor," APL Photonics **6**, 096103 (2021).
[29]Y. Geng, L. A. Schery, R. Sharma, A. Dubra, K. Ahmad, R. T. Libby, and D. R. Williams, "Optical properties of the mouse eye," Biomed. Opt. Express **2**, 717–738 (2011).
[30]M. R. Gardner, A. S. Rahman, T. E. Milner, and H. G. Rylander III, "Scattering-angle-resolved optical coherence tomography of a hypoxic mouse retina model," J. Exp. Neurosci. **13** (2019).
[31]T. Schmoll, A. S. G. Singh, C. Blatter, S. Schriefl, C. Ahlers, U. Schmidt-Erfurth, and R. A. Leitgeb, "Imaging of the parafoveal capillary network and its integrity analysis using fractal dimension," Biomed. Opt. Express **2**, 1159–1168 (2011).
[32]G. Van Rossum and F. L. Drake, *Python 3 Reference Manual* (CreateSpace, Scotts Valley, CA, 2009).
[33]J. D. Hunter, "Matplotlib: A 2D graphics environment," Comput. Sci. Eng. **9**, 90–95 (2007).
[34]C. R. Harris, K. J. Millman, S. J. van der Walt, R. Gommers, P. Virtanen, D. Cournapeau, E. Wieser, J. Taylor, S. Berg, N. J. Smith, R. Kern, M. Picus, S. Hoyer, M. H. van Kerkwijk, M. Brett, A. Haldane, J. F. del Río, M. Wiebe, P. Peterson, P. Gérard-Marchant, K. Sheppard, T. Reddy, W. Weckesser, H. Abbasi, C. Gohlke, and T. E. Oliphant, "Array programming with NumPy," Nature **585**, 357–362 (2020).
[35]G. Bradski, The OpenCV Library, Dr. Dobb's Journal of Software Tools, 2000.
[36]P. Virtanen, R. Gommers, T. E. Oliphant, M. Haberland, T. Reddy, D. Cournapeau, E. Burovski, P. Peterson, W. Weckesser, J. Bright, S. J. van der Walt, M. Brett, J. Wilson, K. J. Millman, N. Mayorov, A. R. J. Nelson, E. Jones, R. Kern, E. Larson, C. J. Carey, İ. Polat, Y. Feng, E. W. Moore, J. VanderPlas, D. Laxalde, J. Perktold, R. Cimrman, I. Henriksen, E. A. Quintero, C. R. Harris, A. M. Archibald, A. H. Ribeiro, F. Pedregosa, P. van Mulbregt, and SciPy 1.0 Contributors, "SciPy 1.0: Fundamental algorithms for scientific computing in Python," Nat. Methods **17**, 261–272 (2020).
[37]J. Schindelin, I. Arganda-Carreras, E. Frise, V. Kaynig, M. Longair, T. Pietzsch, S. Preibisch, C. Rueden, S. Saalfeld, B. Schmid, J.-Y. Tinevez, D. J. White, V. Hartenstein, K. Eliceiri, P. Tomancak, and A. Cardona, "Fiji: An open-source platform for biological-image analysis," Nat. Methods **9**, 676–682 (2012).
[38]P. Thevenaz, U. E. Ruttimann, and M. Unser, "A pyramid approach to subpixel registration based on intensity," IEEE Trans. Image Process. **7**, 27–41 (1998).
[39]R. Haindl, W. Trasischker, B. Baumann, M. Pircher, and C. K. Hitzenberger, "Three-beam Doppler optical coherence tomography using a facet prism telescope and MEMS mirror for improved transversal resolution," J. Mod. Opt. **62**, 1781–1788 (2015).
[40]J. D. Bailoo, E. Murphy, M. Boada-Saña, J. A. Varholick, S. Hintze, C. Baussière, K. C. Hahn, C. Göpfert, R. Palme, B. Voelkl, and H. Würbel, "Effects of cage enrichment on behavior, welfare and outcome variability in female mice," Front. Behav. Neurosci. **12**, 232 (2018).
[41]P. Zhang, J. Mocci, D. J. Wahl, R. K. Meleppat, S. K. Manna, M. Quintavalla, R. Muradore, M. V. Sarunic, S. Bonora, E. N. Pugh, and R. J. Zawadzki, "Effect of a contact lens on mouse retinal *in vivo* imaging: Effective focal length changes and monochromatic aberrations," Exp. Eye Res. **172**, 86–93 (2018).
[42]L. R. Ferguson, S. Balaiya, S. Grover, and K. V. Chalam, "Modified protocol for *in vivo* imaging of wild-type mouse retina with customized miniature spectral domain optical coherence tomography (SD-OCT) device," Biol. Proced. Online **14**, 9 (2012).
[43]M. A. Rauf, J. P. Graham, S. B. Bukallah, and M. A. S. Al-Saedi, "Solvatochromic behavior on the absorption and fluorescence spectra of Rose Bengal dye in various solvents," Spectrochim. Acta, Part A **72**, 133–137 (2009).
[44]B. C. Gilger and R. Stoppini, "Chapter 1—Equine ocular examination: Routine and advanced diagnostic techniques," in *Equine Ophthalmology*, 2nd ed., edited by B. C. Gilger (W. B. Saunders, Saint Louis, 2011), pp. 1–51.
[45]E. I. Alarcon, H. Poblete, H. Roh, J.-F. Couture, J. Comer, and I. E. Kochevar, "Rose Bengal binding to collagen and tissue photobonding," ACS Omega **2**, 6646–6657 (2017).
[46]R. P. Feenstra and S. C. Tseng, "Comparison of fluorescein and Rose Bengal staining," Ophthalmology **99**, 605–617 (1992).
[47]T. Yardeni, M. Eckhaus, H. D. Morris, M. Huizing, and S. Hoogstraten-Miller, "Retro-orbital injections in mice," Lab Anim. **40**, 155–160 (2011).
[48]B. Chang, "Mouse models for studies of retinal degeneration and diseases," Methods Mol. Biol. **935**, 27–39 (2013).
[49]E. L. Fletcher, A. I. Jobling, K. A. Vessey, C. Luu, R. H. Guymer, and P. N. Baird, "Animal models of retinal disease," Prog. Mol. Biol. Transl. Sci. **100**, 211–286 (2011).
[50]A. Stahl, K. M. Connor, P. Sapieha, J. Chen, R. J. Dennison, N. M. Krah, M. R. Seaward, K. L. Willett, C. M. Aderman, K. I. Guerin, J. Hua, C. Löfqvist, A. Hellström, and L. E. H. Smith, "The mouse retina as an angiogenesis model," Invest. Ophthalmol. Visual Sci. **51**, 2813–2826 (2010).
[51]X. Hui, M. O. A. Malik, and M. Pramanik, "Looking deep inside tissue with photoacoustic molecular probes: A review," J. Biomed. Opt. **27**, 070901 (2022).
[52]M. Wang, C. C. C. Corpuz, and F. Zhang, "Shaping eyeballs by scleral collagen cross-linking: A hypothesis for myopia treatment," Front. Med. **8**, 655822 (2021).
[53]V. P. Nguyen, Y. Li, W. Zhang, X. Wang, and Y. M. Paulus, "High-resolution multimodal photoacoustic microscopy and optical coherence tomography image-guided laser induced branch retinal vein occlusion in living rabbits," Sci. Rep. **9**, 10560 (2019).
[54]X.-X. Zhou, Y.-P. Song, Y.-X. Zhao, and J.-G. Wu, "Induction of branch retinal vein occlusion by photodynamic therapy with Rose Bengal in a rabbit model,"

in *Advances in Ophthalmology*, edited by S. Rumelt (IntechOpen, Rijeka, 2012), Chap. 22.
[55]S. Fuma, A. Nishinaka, Y. Inoue, K. Tsuruma, M. Shimazawa, M. Kondo, and H. Hara, "A pharmacological approach in newly established retinal vein occlusion model," Sci. Rep. **7**, 43509 (2017).
[56]V. P. Nguyen, T. Zhu, J. Henry, W. Zhang, X. Wang, and Y. M. Paulus, "Multimodal in vivo imaging of retinal and choroidal vascular occlusion," Photonics **9**, 201 (2022).
[57]K. Hirabayashi, M. Tanaka, A. Imai, Y. Toriyama, Y. Iesato, T. Sakurai, A. Kamiyoshi, Y. Ichikawa-Shindo, H. Kawate, M. Tanaka, K. Dai, N. Cui, Y. Wei, K. Nakamura, S. Iida, S. Matsui, A. Yamauchi, T. Murata, and T. Shindo, "Development of a novel model of central retinal vascular occlusion and the therapeutic potential of the adrenomedullin–receptor activity–modifying protein 2 system," Am. J. Pathol. **189**, 449–466 (2019).
[58]L. T. Watts, W. Zheng, R. J. Garling, V. C. Frohlich, and J. D. Lechleiter, "Rose Bengal photothrombosis by confocal optical imaging in vivo: A model of single vessel stroke," J. Visualized Exp. **100**, e52794 (2015).
[59]C. T. Sullender, A. E. Mark, T. A. Clark, T. V. Esipova, S. A. Vinogradov, T. A. Jones, and A. K. Dunn, "Imaging of cortical oxygen tension and blood flow following targeted photothrombotic stroke," Neurophotonics **5**, 035003 (2018).
[60]T. A. Clark, C. Sullender, S. M. Kazmi, B. L. Speetles, M. R. Williamson, D. M. Palmberg, A. K. Dunn, and T. A. Jones, "Artery targeted photothrombosis widens the vascular penumbra, instigates peri-infarct neovascularization and models forelimb impairments," Sci. Rep. **9**, 2323 (2019).
[61]P. Delafontaine-Martel, C. Zhang, X. Lu, R. Damseh, F. Lesage, and P. J. Marchand, "Targeted capillary photothrombosis via multiphoton excitation of Rose Bengal," J. Cereb. Blood Flow Metab. (published online 2023).
[62]W. Liu and H. F. Zhang, "Photoacoustic imaging of the eye: A mini review," Photoacoustics **4**, 112–123 (2016).
[63]Y. Li and Y. M. Paulus, "Photoacoustic imaging of the eye," in *Photoacoustic Imaging*, edited by R. R. Gharieb (IntechOpen, Rijeka, 2019), Chap. 6.
[64]R. L. Peiffer, L. Pohm-Thorsen, and K. Corcoran, "Chapter 19—Models in ophthalmology and vision research," in *The Biology of the Laboratory Rabbit*, 2nd ed., edited by P. J. Manning, D. H. Ringler, and C. E. Newcomer (Academic Press, San Diego, 1994), pp. 409–433.
[65]V. P. Nguyen, Y. Li, J. Henry, W. Zhang, X. Wang, and Y. M. Paulus, "High resolution multimodal photoacoustic microscopy and optical coherence tomography visualization of choroidal vascular occlusion," Int. J. Mol. Sci. **21**, 6508 (2020).
[66]Y. Li, W. Zhang, V. P. Nguyen, R. Rosen, X. Wang, X. Xia, and Y. M. Paulus, "Real-time OCT guidance and multimodal imaging monitoring of subretinal injection induced choroidal neovascularization in rabbit eyes," Exp. Eye Res. **186**, 107714 (2019).
[67]V. P. Nguyen, Y. Li, W. Qian, B. Liu, C. Tian, W. Zhang, Z. Huang, A. Ponduri, M. Tarnowski, X. Wang, and Y. M. Paulus, "Contrast agent enhanced multimodal photoacoustic microscopy and optical coherence tomography for imaging of rabbit choroidal and retinal vessels *in vivo*," Sci. Rep. **9**, 5945 (2019).
[68]V. P. Nguyen, Y. Li, M. Aaberg, W. Zhang, X. Wang, and Y. M. Paulus, "In vivo 3D imaging of retinal neovascularization using multimodal photoacoustic microscopy and optical coherence tomography imaging," J. Imaging **4**, 150 (2018).
[69]C. Tian, W. Zhang, A. Mordovanakis, X. Wang, and Y. M. Paulus, "Noninvasive chorioretinal imaging in living rabbits using integrated photoacoustic microscopy and optical coherence tomography," Opt. Express **25**, 15947–15955 (2017).
[70]W. Zhang, Y. Li, V. P. Nguyen, Z. Huang, Z. Liu, X. Wang, and Y. M. Paulus, "High-resolution, in vivo multimodal photoacoustic microscopy, optical coherence tomography, and fluorescence microscopy imaging of rabbit retinal neovascularization," Light: Sci. Appl. **7**, 103 (2018).
[71]W. Song, Q. Wei, T. Liu, D. Kuai, J. M. Burke, S. Jiao, and H. F. Zhang, "Integrating photoacoustic ophthalmoscopy with scanning laser ophthalmoscopy, optical coherence tomography, and fluorescein angiography for a multimodal retinal imaging platform," J. Biomed. Opt. **17**, 061206 (2012).
[72]M. R. Gardner, N. Katta, A. S. Rahman, H. G. Rylander, and T. E. Milner, "Design considerations for murine retinal imaging using scattering angle resolved optical coherence tomography," Appl. Sci. **8**, 2159 (2018).
[73]Q. Li, A. M. Timmers, K. Hunter, C. Gonzalez-Pola, A. S. Lewin, D. H. Reitze, and W. W. Hauswirth, "Noninvasive imaging by optical coherence tomography to monitor retinal degeneration in the mouse," Invest. Ophthalmol. Visual Sci. **42**, 2981–2989 (2001).
[74]M. T. Pardue, R. A. Stone, and P. M. Iuvone, "Investigating mechanisms of myopia in mice," Exp. Eye Res. **114**, 96–105 (2013).
[75]X. Zhou, J. Xie, M. Shen, J. Wang, L. Jiang, J. Qu, and F. Lu, "Biometric measurement of the mouse eye using optical coherence tomography with focal plane advancement," Vision Res. **48**, 1137–1143 (2008).
[76]K. H. Kim, M. Puoris'haag, G. N. Maguluri, Y. Umino, K. Cusato, R. B. Barlow, and J. F. de Boer, "Monitoring mouse retinal degeneration with high-resolution spectral-domain optical coherence tomography," J. Vision **8**, 17 (2008).
[77]L. M. Serfilippi, D. R. S. Pallman, M. M. Gruebbel, T. J. Kern, and C. B. Spainhour, "Assessment of retinal degeneration in outbred albino mice," Comp. Med. **54**, 69–76 (2004).
[78]D. Cherfan, E. E. Verter, S. Melki, T. E. Gisel, F. J. Doyle, Jr., G. Scarcelli, S. H. Yun, R. W. Redmond, and I. E. Kochevar, "Collagen cross-linking using Rose Bengal and green light to increase corneal stiffness," Invest. Ophthalmol. Visual Sci. **54**, 3426–3433 (2013).